

CrossMark
click for updates

Cite this: DOI: 10.1039/c5ta03893f

Improved electrochemical performance of tin-sulfide anodes for sodium-ion batteries†

Ying Ching Lu,^a Chuze Ma,^c Judith Alvarado,^c Nikolay Dimov,^b Ying Shirley Meng^c and Shigeto Okada^{*b}

Due to their highly reversible capacity, tin-sulfide-based materials have gained attention as potential anodes for sodium-ion and lithium-ion batteries. Nevertheless, the performance of tin sulfide anodes is much lower than that of tin oxide anodes. The aim of the present investigation is to improve the electrochemical performances of SnS anodes for sodium-ion batteries using conventional organic electrolytes. Three different carbon composite anodes, SnS/reduce graphene oxide (SnS/G), SnS/reduce graphene oxide/hard carbon (SnS/G + C), and SnS/hard carbon (SnS/C), were prepared by hot water bath synthesis followed by mechanical milling. The mechanism of the conversion and alloying reaction was investigated by TEM. The feasibility of SnS anodes was confirmed in a full cell configuration using Na₃V₂(PO₄)₂F₃ as the cathode.

Received 29th May 2015
Accepted 24th June 2015

DOI: 10.1039/c5ta03893f

www.rsc.org/MaterialsA

Introduction

Following their commercialization in 1991, Li-ion batteries (LIBs) have been widely adopted for portable electronic devices and electric vehicles. Quickly this technology has become ubiquitous in societies' daily life. Although initially LIBs have been used in portable electronic devices, their use has extended to large-scale applications such as battery-assisted bicycles and electric vehicles. The advantages of LIBs over nickel-hydride and lead-acid batteries are high cell voltage and high energy density. In addition, due to their high charge/discharge efficiency and long cycle life, LIBs have recently been considered as a temporary energy storage system for unstable renewable energy sources. However, the limited lithium resources and high cost are drawbacks for large-scale applications. For this reason, Na-ion batteries (SIBs) have recently gained attention as a potential alternative to LIBs because of their lower cost and similar electrochemical behavior to LIBs. Nevertheless, potential electrode candidates for SIBs are limited by the large ionic radius of Na. Some carbonaceous anodes have been investigated for SIBs using a similar analogy to LIBs.^{1,2} Some hard carbon anodes have exhibited low irreversible capacity, low polarization, and good cycling performance. However, thus far,

the maximum rechargeable capacity of a hard carbon anode for sodium-ion batteries has been less than *ca.* 320 mA h g⁻¹.³⁻⁵ On the other hand, several transition metal oxides⁶⁻⁹ have been reported as possible cathode candidates for SIBs. Recently, several Na alloy anodes, such as tin (Sn),^{10,11} antimony (Sb),^{12,13} phosphorus (P),^{14,15} have been proposed to improve the rechargeable capacity. Among these, Sn is a very promising anode material candidate for SIB anodes due to its high theoretical capacity (Na₁₅Sn₄: 854 mA h g⁻¹), good chemical stability, and low toxicity. However, the operating voltage is extremely close to the Na plating/stripping potential. Moreover, the large volume change and particle agglomeration during the charge and discharge cause capacity degradation of the metallic Sn. To reduce the volume change and prevent the particle agglomeration of Sn, several compounds and nanostructures have been proposed.¹⁶⁻¹⁸ Recently, tin oxides (SnO and SnO₂) were investigated as anode active materials for SIBs.^{19,20} In the initial cycle, the tin oxides were reduced by Na, generating Sn and Na₂O, the latter which forms during the conversion reaction can prevent the agglomeration of Sn particles and reduce the volume expansion of Sn. In our previous work, we compared the electrochemical performance of SnO and SnO₂ and found that the bulk conductivity of the anode active material plays an important role in the electrochemical performance.²¹ Based on our previous results, tin sulfide should be a more promising anode material than tin oxide. Tin sulfide undergoes a similar first cycle conversion reaction (SnS + 2Na⁺ + 2e⁻ → Sn + Na₂S). Nevertheless, the reported tin sulfide anode performance is significantly lower than that of tin oxide anode. L. Wu has reported that a Sn-SnS-C nanocomposite anode delivered 90% capacity retention for over 150 cycles against sodium.²² X. Xie, T. B. Qu and Y. Liu have integrated SnS₂ and reduced graphene

^aDepartment of Chemical Engineering, Interdisciplinary Graduate School of Engineering Sciences, Kyushu University, Fukuoka 819-0395, Japan

^bInstitute for Materials Chemistry and Engineering, Kyushu University, Fukuoka 816-8580, Japan. E-mail: s-okada@cm.kyushu-u.ac.jp; Fax: +81 92 583 7841; Tel: +81 92 583 7841

^cDepartment of NanoEngineering, University of California San Diego, La Jolla, CA 92037, USA

† Electronic supplementary information (ESI) available. See DOI: 10.1039/c5ta03893f

oxide (SnS₂@graphene), resulting in excellent reversible capacity with more than 630 mA h g⁻¹.^{23–25} T. Zhou tried thermal treatment to transform SnS₂@graphene into SnS@graphene and demonstrated that SnS@graphene had an improved anode performance, delivering 940 mA h g⁻¹ at 30 mA g⁻¹. After 250 cycles SnS@graphene showed 492 and 308 mA h g⁻¹ at the current densities of 810 and 7290 mA g⁻¹, respectively.²⁶ Herein, we aimed to synthesize new SnS anode composites using various carbon-based materials such as graphene oxide (GO) to improve the cycling performance and rate capability of SIBs. Moreover, the reasons for the capacity degradation in SnS anodes are discussed.

Experimental

Synthesis of bare SnS and SnS/C

SnS was prepared by using a hot water bath. 0.75 g SnCl₂·H₂O (Sigma-Aldrich; 98% purity) was dissolved in 50 ml 0.25 M citric acid (Wako Pure Chemical Industries, Ltd.), which was used as an antioxidant to prevent the oxidation of Sn ions from Sn²⁺ to Sn⁴⁺. Approximately 20% aqueous ammonia solution was added dropwise to adjust the solution pH to 5. Then 0.25 g thioacetamide (CH₃CSNH₂, Wako Pure Chemical Industries, Ltd.) was added as a sulfur source (molar ratio of Sn : S = 1 : 1), and then the solution was stirred and heated at 80 °C. After immersion in a hot water bath, the sample was washed with distilled water and ethanol (EtOH) several times to remove contaminants and dried at 80 °C overnight. Finally, the sample was treated at 450 °C for 3 hours in an inert environment to obtain bare SnS. The composite of SnS and hard carbon (SnS/C) was prepared by mechanical milling. The SnS prepared in the hot water bath was mixed with hard carbon (Carbotron P(f); Kureha Corp.) by mechanical milling at 400 rpm for 1 hour. The nominal weight ratio of SnS to hard carbon was 8 : 2.

Synthesis of SnS/G and SnS/G + C

First, GO was prepared by Hummers' method with modifications.²⁷ 0.15 g GO sheets were separated one by one in 100 ml distilled water (1.5 mg ml⁻¹) by sonication. After sonication, the separated GO sheets were dissolved in 7.2 g citric acid (0.75 M). Then, 0.75 g SnCl₂·H₂O with some ammonia hydroxide were added to adjust the solution pH to 5. Because the Sn²⁺ ions would be oxidized by GO²⁸ and citric acid could not totally prevent the oxidization of Sn²⁺ ions, the Sn : S molar ratio was adjusted to 1 : 1.4 (0.375 g thioacetamide). After the hot water bath (80 °C for 12 h), samples were treated at 650 °C for 3 hours under Ar gas to remove the SnS₂ and obtain SnS/G. SnS/G + C was prepared in a similar manner to SnS/C, using mechanical milling at 400 rpm for 1 h. The nominal weight ratio of SnS/G to hard carbon was 9 : 1.

Samples were analyzed by X-ray diffraction with a 15 kW high-brilliance Cu-K α rotating anode (XRD; Rigaku TTRIII). The particle size and particle morphology were observed by using a field emission scanning electron microscope (FESEM; JEOL JSM-6340F/5310) and a transmission electron microscope (TEM; JEOL JEM 2100F). The carbon content in the SnS/G

composite was measured by thermogravimetry (TG; Rigaku Thermo Plus TG8210).

Electrochemical measurements in a half cell

Electrodes were prepared by mixing appropriate amounts of the active material/acetylene black (AB) mixture with a 2 wt% DI water–absolute alcohol mixture (4 : 1 by weight ratio) of carboxymethyl cellulose (CMC) (MW = 700 000; Sigma-Aldrich). The ingredients were added to a polypropylene vial containing 3 g of zirconia balls (3 mm ϕ). The vials were then placed in a rocking mill (Seiwa Giken Co., Ltd.) and mixed for 60 min at 50 Hz to form a slurry. Then the slurry was coated onto a 20 μ m Cu foil current collector by using the doctor blade technique and dried under vacuum at 80 °C overnight. Electrochemical tests were carried out in two-electrode 2032 coin cells (Hohsen Corp.). Sodium metal foil was used as a counter electrode. Both the working electrode and counter electrode were punched to 15 mm ϕ . The loading mass of the active material in the electrode was 2.0 (\pm 0.05) mg for a half cell. 1 M NaPF₆ dissolved in ethylene carbonate (EC) and propylene carbonate (PC) 1 : 1 by volume (Tomiyama Pure Chemical Industries, Ltd.) was used as an electrolyte. The separator was a GF/A glass fiber filter paper (Whatman). Cycle life and rate performance testing experiments were performed at different current densities in the voltage range of 2.0 V–0.01 V. Cyclic voltammetry (CV) was conducted on a VersaSTAT 3 (Princeton Applied Research) at a scan rate of 0.05 mV s⁻¹.

Electrochemical measurements in a full cell

A full cell test was carried out in a two-electrode 2032 coin cell. Na₃V₂(PO₄)₂F₃ mixed with AB and polytetrafluoroethylene (PTFE) was used as the cathode (70 : 25 : 5 in weight). SnO and SnS/G + C were used as anodes and were prepared using the same procedures as for the half-cell. SnO was prepared by the hydrothermal method as previously reported.¹⁷ Both the cathode and anode were punched to 10 mm ϕ . The loading amount of the active material in the electrode was 1.0 (\pm 0.05) mg for the full cell. The separator was a GF/A glass fiber filter paper (Whatman) and the electrolyte was 1 M NaPF₆ dissolved in ethylene carbonate (EC) and diethylene carbonate (DEC) 1 : 1 by volume (Tomiyama Pure Chemical Industries, Ltd.). The voltage ranges of the full cells were between 3.7 V and 1.2 V (Na₃V₂(PO₄)₂F₃//SnO) and 3.6 V–1.1 V (Na₃V₂(PO₄)₂F₃//SnS/G + C), respectively. The current density of the full cells was tested at a current density of 0.2 mA cm⁻² (257 mA g⁻¹).

Results and discussion

Material characteristics of SnS

Fig. 1 shows the XRD patterns of bare SnS and SnS/G before and after thermal treatment. In Fig. 1(b), the peaks located at $2\theta = 14.9^\circ$ and 28.6° could be indexed to SnS₂ (ICCD 023-0677), suggesting that some of the Sn²⁺ ions were oxidized to Sn⁴⁺ during the hot water bath. This phenomenon was also reported by M. Zhang.²⁸ After thermal treatment, all of the high crystallinity peaks in Fig. 1(c) could be indexed to SnS.

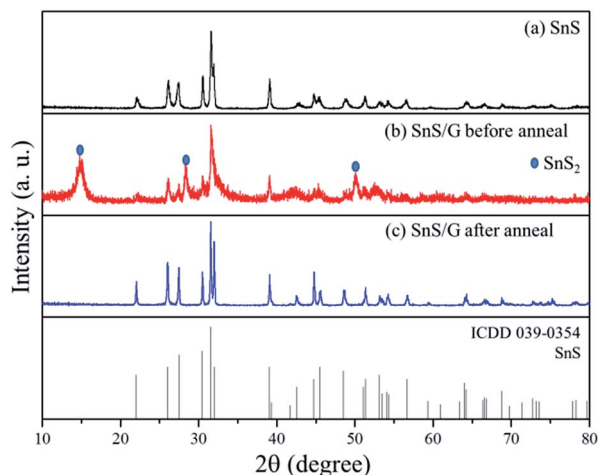


Fig. 1 XRD patterns of: (a) bare SnS, (b) SnS/G before annealing and (c) SnS/G after annealing.

The XPS measurement results are shown in Fig. 2. In Fig. 2(a), the XPS spectrum showed the GO peaks at 284.1 eV, 285.9 eV, 287.9 eV, and 289.5 eV, which corresponded to the C–C bond, C–O bond, C=O bond and O–C=O bond, respectively.^{29,30} In the C1s XPS spectrum of SnS/G, the C–C bonds were more intense than the covalent bonds of carbon and oxygen (Fig. 2(b)), suggesting that most of the oxygen functional groups were removed by the hot water bath and thermal treatment. The Sn 3d_{5/2} peak of SnS/G was located at 486.7 eV corresponding to SnS (Fig. 2(c)),^{26,31} suggesting that the SnS₂ impurities decomposed to SnS after the thermal treatment, which agreed with the XRD results.

The morphologies of SnS and SnS/G before and after thermal treatment are shown in Fig. 3. The SnS particles have a layered structure with random particle size, and the SnS layer thickness of about 200 nm (Fig. 3(a)). Before thermal treatment, the SnS/G material formed a beehive-like porous structure (Fig. 3(b)). After

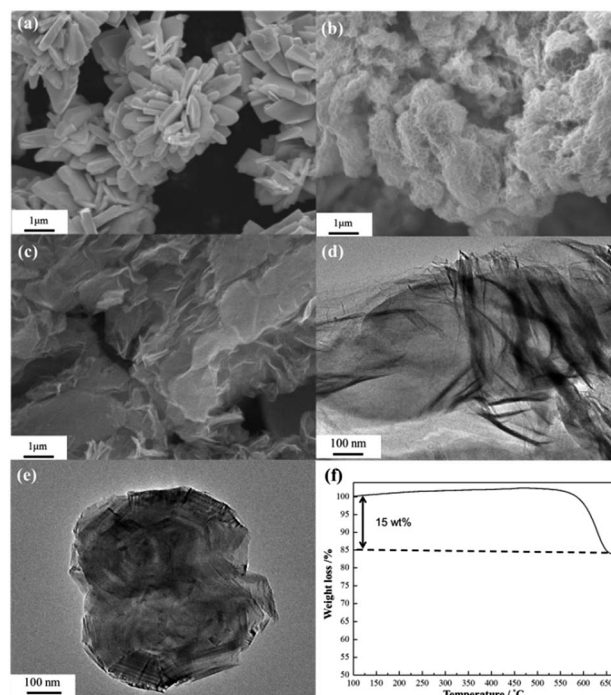


Fig. 3 (a) SEM images of bare SnS, (b) SEM images of SnS/G before annealing, (c) SEM images of SnS/G after annealing, (d) TEM images of SnS/G, (e) TEM images of a SnS single particle in SnS/G, and (f) TG curve of the SnS/G sample heated in air at 5 °C min⁻¹.

thermal treatment (Fig. 3(c)), the SnS/G lost its original shape and the SnS particles were covered by a graphene nanosheet.

To confirm the morphology of the SnS particles in the SnS/G, the SnS/G powder was dispersed in ethanol, and then sonication was applied to separate the SnS particles from the graphene nanosheet. The SnS showed a plate-like structure forming sheet-like SnS (Fig. 3(e)). The TG data in Fig. 3(f) show that the weight ratio of SnS : reduced graphene oxide (RGO) is 85 : 15. The TG profile was measured to 700 °C at a heating rate of 10 °C min⁻¹ in air. The carbon content of the different carbon composite samples is shown in Table 1.

Electrochemical measurements in a half cell

The electrochemical behavior of SnS against Na was characterized by cyclic voltammetry (Fig. 4(a)). The strong peak at 0.7 V, which was only observed in the initial cathodic curve, was attributed to the formation of a solid electrolyte interphase (SEI) layer. From the third cycle the CV curve became stable, suggesting that the SEI layer became stable. The oxidation/

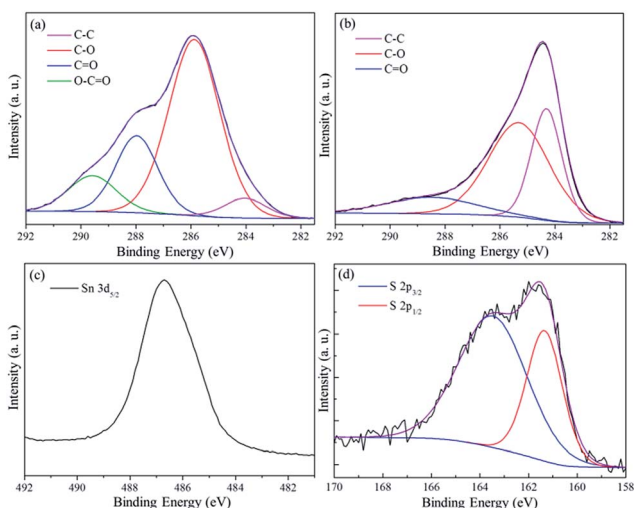


Fig. 2 XPS patterns of: (a) C 1s of graphene oxide, (b) C 1s of SnS/G, (c) Sn 3d of SnS/G, and (d) S 2p of SnS/G.

Table 1 SnS : carbon ratio in the different carbon composited samples

Anode	SnS	Carbon
SnS/G	85%	15% (RGO)
SnS/G + C	76.5%	13.5% (RGO), 10% (hard carbon)
SnS/C	80%	20% (hard carbon)

reduction pairs at 0.1/0.02 V, 0.13/0.23 V, and 0.61/0.63 V were attributed to alloying and dealloying reactions between Sn and Na.^{22–26} The reduction peak at 1.15 V was caused by the conversion reaction between SnS and Na. The oxidation peak at 1.34 V and the broad peak at about 1.73 V were attributed to the reconversion reaction between the Sn and Na₂S.^{22,26}

Fig. 4(b) shows the charge/discharge profiles of the first two cycles for the bare SnS, SnS/G, SnS/G + C, and SnS/C anodes at a current density of 50 mA g⁻¹. The reversible capacities of the first cycle were 621, 638, 598 and 511 mA h g⁻¹ with coulombic efficiencies of 66.2%, 80.4%, 78.2%, and 71.3%, respectively.

Fig. 4(c) compares the cycling performance of the SnS, SnS/G, SnS/G + C, and SnS/C anodes. Compared to the bare SnS sample, all carbon composite samples showed lower polarization, better capacity retention, and higher coulombic efficiency. The SnS/G + C sample especially showed the best performance among the carbon composite anode electrodes.

Fig. 4(d) shows the rate capability of the SnS/G + C and SnS/C anodes. Both showed good rate capability even at high charge/discharge rates. The SnS/C anode delivered 506, 474, 424 and 320 mA h g⁻¹ at a rate of 50, 100, 200, and 500 mA g⁻¹, respectively. In contrast, the SnS/G + C anode delivered 590 mA h g⁻¹ at 50 mA g⁻¹ and showed 458 mA h g⁻¹ even at 500 mA g⁻¹. The higher rate capability of SnS/G + C seems to be due to the high conductivity of the RGO.

Though SnS/G + C showed good cycle and rate performance as a potential anode material for Na-ion batteries, pairing with a cathode material to make a full cell introduces new challenges. Our previously reported Na₃V₂(PO₄)₂F₃ (NVPF) active material was used as the cathode³² and was paired with SnS/G + C to test the electrochemical performance of a full cell. To further examine the relationship between the electrochemical performance and conductivity of the anode active material, our previously reported SnO (cite) was also paired with the NVPF cathode. Considering the irreversible capacity in the first cycle of SnO and SnS/G + C, the NVPF//SnO cell and NVPF//SnS/G + C cell were prepared under cathode-rich conditions (NVPF : SnO = 7 : 1; NVPF : SnS/G + C = 8 : 1 in weight). The electrochemical properties of NVPF are shown in Fig. S1.†

Electrochemical measurements in a full cell

The charge/discharge profiles in the selected cycle and cycling performance of the full cells are shown in Fig. 5. Both the NVPF//SnO cell and NVPF//SnS/G + C cell showed good performance, with capacity retentions of 154.4% and 86.3% in 50 cycles. The initial charge/discharge capacities of the NVPF//SnO cell and NVPF//SnS/G + C cell were 322/95 mA h g⁻¹ and 504/319 mA h g⁻¹, with the coulombic efficiencies of 29.5% and 63.4%, respectively. As expected, the SnS/G + C anode outperformed the SnO anode in the full cell configuration.

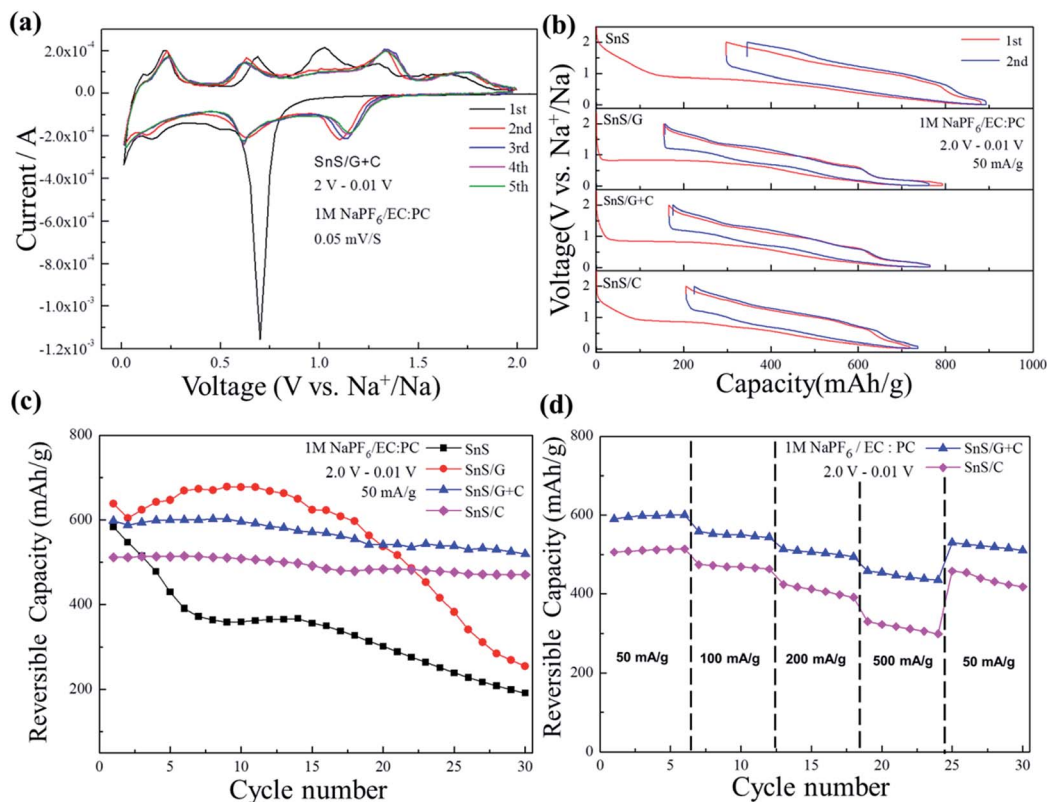


Fig. 4 (a) Cyclic voltammograms for the first five cycles of the SnS/G + C anode at a scanning rate of 0.05 mV s⁻¹, (b) charge/discharge profiles of bare SnS, SnS/G, SnS/G + C, and SnS/C anodes, (c) cyclabilities of bare SnS, SnS/G, SnS/G + C and SnS/C anodes, and (d) rate capabilities of SnS/G + C and SnS/C anodes.

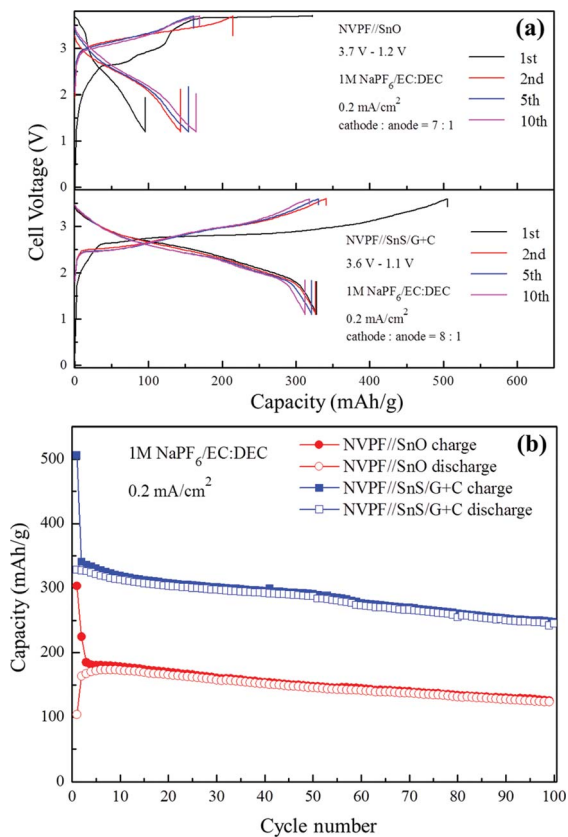


Fig. 5 (a) Voltage profile and (b) cyclabilities of NVPF//SnO and NVPF//SnS/G + C cells.

The capacity fading mechanism of the SnS anodes was further studied by TEM. SnS anodes in their fully discharged and charged states were examined. Fig. 6 shows the TEM image of the fully sodiated SnS/G + C electrode. The first cycle conversion reaction transforms the plate-like pristine SnS to particles with an irregular shape (Fig. 6(a)). The nanoparticles that were distributed throughout the amorphous matrix correspond to the Sn or Na_xSn nanoparticles generated from SnS after the conversion reaction (Fig. 6(b)). This result is very similar to the converted SnO₂ studied in our previously reported work.²¹ The fully disodiated SnS/G + C is shown in Fig. 6(c) and (d). After the full charge, the primary particles disintegrated into nanoparticles around 5 nm. Although SnS in the SnS/G + C completely lost its shape, it still shows evenly dispersed particles without any Sn particle agglomeration. This is consistent with the high coulombic efficiencies of SnS/G and SnS/G + C shown in Fig. 4(b). The scheme of the morphological changes is shown in Fig. S2.†

Fig. 7(a) and (c) compare the voltage profile and cycling performance of SnS/C at different cutoff voltages. In Fig. 7(c), cutting of the voltage at 1.5 V for SnS/C demonstrates good stability to the tenth cycle. However, after the tenth cycle the capacity gradually decays. In contrast, if the sample is cutoff at 2 V, the cell exhibited stable capacity over 30 cycles. Comparing the voltage profile shown in Fig. 7(a), the sample with a cutoff at 2 V showed a stable charge/discharge curve in each cycle, in

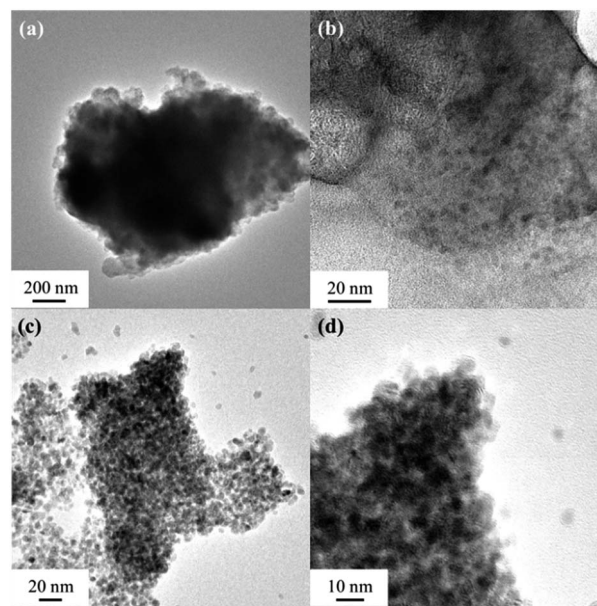


Fig. 6 TEM images: (a) and (b) SnS/G + C electrode after full charge (sodiated); (c) and (d) SnS/G + C electrode after full discharge (disodiated).

contrast, the voltage curve of the sample with cutoff at 1.5 V showed degradation in each cycle. The SnS/C electrodes at various cutoff voltages after the 30th cycle were observed by SEM (Fig. S3(a)–(d)†). In Fig. S3(a) and (b),† the samples that were cutoff at 1.5 V showed cracks and crumbled after the 30th cycle. In contrast, the sample charged to 2 V was stable and still maintained the electrode integrity over 30 cycles (Fig. S3(c) and (d)†). Here the fiber-like structure corresponds to the glass fiber separator. These data could be explained by the incomplete reconversion reaction if reducing the cut-off voltage (reducing the conversion reaction driving force) and the incomplete reconversion reaction could cause the cracking of the Na₂S buffer layer during the cycles.

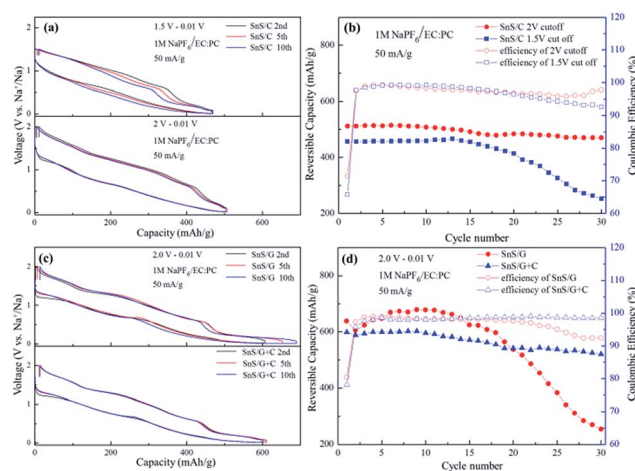
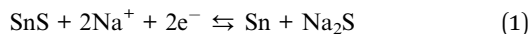


Fig. 7 Voltage profile in the selected cycles, cyclabilities and coulombic efficiencies of (a), (b) SnS/C at different cutoff voltages (c), and (d) SnS/G and SnS/G + C.

Fig. 7(b) and (d) show the charge/discharge profile for selected cycles. As demonstrated, SnS/G + C have a very stable charge/discharge curve for each cycle. The SnS/G + C also showed a stable electrode structure even after 30 cycles (Fig. S3(g) and (h)†). During the discharge and charge process, the Na ions were reversibly reacted with SnS to form Na_xSn and Na₂S:



A large volume change occurs during the alloy reaction. The SnS/G + C in particular show a high conversion reversibility, shown in Fig. 7(c). The capacity degradation of the SnS/G might be attributed to the large volume change due to the cracking and substrate lift off from the current collector. However, mixing hard carbon through ball milling can separate the SnS/G into the matrix of hard carbon. This can further reduce the volume expansion and eliminate the stress during the charge/discharge process. Through this reasoning the improved cycle performance of SnS/G + C and SnS/C samples can be explained.

To sum up the results shown in Fig. 7 and S3,† the capacity degradation in the bare SnS could be attributed to the following factors; (1) large volume change during the charge/discharge process; and (2) the incomplete reconversion reaction due to the cracking of the Na₂S buffer layer. Reconversion reactions must overcome the lattice energy and the poor conductivity of the Na compounds (such as Na₂S and Na₂O) in order to reverse the transformation reaction. As shown in Fig. 4(b), SnS/G, SnS/G + C and SnS/C showed lower polarization than the bare SnS, suggesting that the conductivity improved after the carbon composition. The distributions of Sn nanoparticles may also play an important role in the reversibility of the conversion reaction. The Sn nanoparticles are highly distributed in Fig. 6(b), suggesting that there was a high contact area between Sn and Na₂S. This was beneficial for increasing the conversion activity of the reverse transformation reaction³³ and can also explain the lower electrochemical performance of the NVPF//SnO. Moreover, NVPF//SnO has a lower carbon content and conductivity, worse distribution,²¹ and higher Na₂O lattice energy (the lattice energy of Na₂O was 2481 kJ mol⁻¹, versus 2203 kJ mol⁻¹ for Na₂S).

Conclusions

In this study hard carbon and RGO were used to improve the cycling performance of SnS anodes. Three different carbon composite samples, SnS/G, SnS/G + C, and SnS/C, were prepared by means of a hot water bath and mechanical milling. All of the materials showed lower polarization and better cycling performance than the bare SnS. Among these carbon composited samples, SnS/G + C exhibited the best cycle performance and rate capability. Based on the TEM image of SnS/G + C after the full charge/discharge states, the cycling performance of SnS/C in different voltage ranges, and the comparison of the charge/discharge voltage profiles of SnS/G and SnS/G + C at elected cycles, we conclude that the capacity degradation of the bare

SnS is attributed to the large volume change. Moreover, the incomplete reversibility of the conversion is due to the cracking of the Na₂S buffer layer. In the full cell test, NVPF//SnS/G + C showed better electrochemical performance than the NVPF//SnO cells. As expected, these results suggest that the conductivity plays an important role in the electrochemical performance of Naion batteries.

Acknowledgements

This work was financially supported by the Elements Science & Technology Projects of MEXT, Japan. C. Z. Ma, J. Alvarado and Y. S. Meng acknowledge funding support from the USA National Science Foundation under Award Number DMR1057170.

Notes and references

- M. M. Doeff, Y. P. Ma, S. J. Visco and L. C. Dejonghe, *J. Electrochem. Soc.*, 1993, **140**, L169.
- R. Alcantara, J. M. Jimenez-Mateos, P. Lavela and J. L. Tirado, *Electrochem. Commun.*, 2001, **3**, 639.
- D. A. Stevens and J. R. Dahn, *J. Electrochem. Soc.*, 2000, **147**, 1271.
- S. Komaba, W. Murata, T. Ishikawa, N. Yabuuchi, T. Ozeki, T. Nakayama, A. Ogata, K. Gotoh and K. Fujiwara, *Adv. Funct. Mater.*, 2011, **21**, 3859.
- J. Zhao, L. Zhao, K. Chihara, S. Okada, J. Yamaki, S. Matsumoto, S. Kuze and K. Nakane, *J. Power Sources*, 2013, **244**, 752.
- J. J. Braconnier, C. Delmas, C. Fouassier and P. Hagemmuller, *Mater. Res. Bull.*, 1980, **15**, 1797.
- S. Okada, Y. Takahashi, T. Kiyabu, T. Doi, J.-I. Yamaki and T. Nishida, *Extended Abstracts of 210th ECS Meeting at Cancun*, 2006, B2, #201.
- J. Zhao, J. Xu, D. H. Lee, N. Dimov, Y. S. Meng and S. Okada, *J. Power Sources*, 2014, **264**, 235.
- J. Xu, D. H. Lee and Y. S. Meng, *Funct. Mater. Lett.*, 2013, **6**, 1330001.
- S. Komaba, Y. Matsuura, T. Ishikawa, N. Yabuuchi, W. Murata and S. Kuze, *Electrochem. Commun.*, 2012, **21**, 65.
- L. Xiao, Y. Cao, J. Xiao, W. Wang, L. Kovarik, Z. Niea and J. Liu, *Chem. Commun.*, 2012, **48**, 3321.
- A. Darwiche, C. Marino, M. T. Sougrati, B. Fraise, L. Stievano and L. Monconduit, *J. Am. Chem. Soc.*, 2012, **134**(51), 20805.
- J. Qian, Y. Chen, L. Wu, Y. Cao, X. Ai and H. Yang, *Chem. Commun.*, 2012, **48**, 7070.
- J. Qian, X. Wu, Y. Cao, X. Ai and H. Yang, *Angew. Chem., Int. Ed.*, 2013, **52**, 4633.
- Y. Kim, Y. Park, A. Choi, N. Choi, J. Kim, J. Lee, J. H. Ryu, S. M. Oh and K. T. Lee, *Adv. Mater.*, 2013, **25**, 3045.
- M. K. Datta, R. Epur, P. Saha, K. Kadakia and S. K. Park, *J. Power Sources*, 2013, **225**, 316.
- H. Zhu, Z. Jia, Y. Chen, N. Weadock, J. Wan, O. Vaaland, X. Han, T. Li and L. Hu, *Nano Lett.*, 2013, **13**, 3093.
- Y. Xu, Y. Zhu, Y. Liu and C. Wang, *Adv. Energy Mater.*, 2012, **3**, 128.

- 19 D. Su, X. Xie and G. Wang, *Chem.–Eur. J.*, 2014, **20**, 3192.
- 20 D. Su, C. Wang, H. Ahnc and G. Wang, *Phys. Chem. Chem. Phys.*, 2013, **15**, 12543.
- 21 Y. C. Lu, C. Ma, J. Alvarado, T. Kidera, N. Dimov, Y.-S. Meng and S. Okada, *J. Power Sources*, 2015, **284**, 287.
- 22 L. Wu, X. Hu, J. Qian, F. Pei, F. Wu, R. Mao, X. Ai, H. Yang and Y. Cao, *J. Mater. Chem. A*, 2013, **1**, 718.
- 23 X. Xie, D. Su, S. Chen, J. Zhang, S. Dou and G. Wang, *Chem.–Asian J.*, 2014, **9**, 1611.
- 24 B. Qu, C. Ma, G. Ji, C. Xu, J. Xu, Y. S. Meng, T. Wang and J. Y. Lee, *Adv. Mater.*, 2014, **26**, 3854.
- 25 Y. Liu, H. Kang, L. Jiao, C. Chen, K. Cao, Y. Wang and H. Yuan, *Nanoscale*, 2015, **7**, 1325.
- 26 T. Zhou, W. K. Pang, C. Zhang, J. Yang, Z. Chen, H. K. Liu and Z. Guo, *ACS Nano*, 2014, **8**, 8323.
- 27 W. S. Hummers and R. E. Offeman, *J. Am. Chem. Soc.*, 1958, **80**, 1339.
- 28 M. Zhang, D. Lei, X. Yu, L. Chen, Q. Li, Y. Wang, T. Wang and G. Cao, *J. Mater. Chem.*, 2012, **22**, 23091.
- 29 H. Shin, K. Kim, A. Benayad, S. Yoon, H. Park, I. Jung, M. Jin, H. Jeong, J. Kim, J. Choi and Y. Lee, *Adv. Funct. Mater.*, 2009, **19**, 1987.
- 30 Z. S. Wu, W. Ren, L. Gao, B. Liu, C. Jiang and H. M. Cheng, *Carbon*, 2009, **47**, 493.
- 31 G. H. Yue, Y. D. Lin, X. Wen, L. S. Wang, Y. Z. Chen and D. L. Peng, *Appl. Phys. A*, 2012, **106**, 87.
- 32 K. Chihara, A. Kitajou, I. D. Gocheva, S. Okada and J. Yamaki, *J. Power Sources*, 2013, **227**, 80.
- 33 T. Li, Z. X. Chen, X. P. Ai, Y. L. Cao and H. X. Yang, *J. Power Sources*, 2012, **217**, 54.